Decomposition phenomena of $Zn_{13-\delta}Sb_{10}$ under working conditions of thermoelectric generators and minimum current densities for electromigration

*Matthias Jakob[‡], Maxim Grauer[‡], Pawel Ziolkowski[§], Oliver Oeckler[‡]**

‡ Institute for Mineralogy, Crystallography and Materials Science; Faculty of Chemistry and Mineralogy, Leipzig University, Scharnhorststraße 20, 04275 Leipzig, Germany

§ Institute of Materials Research, Linder Höhe, German Aerospace Center, 51170 Cologne, Germany

Thermoelectrics, $Zn_{13-x}Sb_{10}$, material degradation, electromigration, Zn mobility

Abstract The mixed ionic-electronic conductor (MIEC) $Zn_{13-\delta}Sb_{10}$ is a thermoelectric material with high performance at intermediate temperatures and contains only abundant elements. This work evaluates its suitability for thermoelectric applications with respect to thermal instability and decomposition by electromigration of Zn under current flow. In addtion to the formation of Zn whiskers, this migration often leads to cracks. Thermoelectric measurements of bulk $Zn_{13-\delta}Sb_{10}$ ($\delta \sim 0.2$) prepared by a slow cooling method show zT values of 0.7 at 200 °C. A series of tests under flowing currents with different voltages and current densities on bar-shaped samples was followed by the space-resolved investigation of their composition and its systematical

correlation with the Seebeck coefficient. The latter increases upon Zn depletion, especially when ZnSb is formed. At RT, Zn migration starts a voltage of ~0.01 V, which is much lower than for other MIECs like copper chalcogenides. At higher electrical fields, which may be enhanced by the Seebeck voltage, the amount of deposited Zn at the negative pole increases with the current density even if the transported charge is kept constant.

1. Introduction

Lowering the thermal conductivity κ of bulk materials is a key objective in thermoelectrics.[1-3] Since the electronic contribution to κ is coupled with electrical conductivity σ according to the Wiedemann-Franz relationship, this approach is mainly limited to suppressing the phononic part of thermal conductivity κ_{ph} in order to enhance the efficiency of energy conversion. To this end, different strategies have been developed in the past years. The phonon-glass electron-crystal (PGEC)[4] concept aims at lowering κ_{ph} close to the value of glasses by introducing a plethora of real-structure effects into crystal structures. This includes disorder on the atomic scale, both static as well as dynamic, i.e. by rattling atoms in large voids that may enhance phonon scattering. Highlights of this concept include, for instance, filled skutterudites [5] or designed grain boundaries in half-Heusler alloys,[6] where charge carrier transport remains almost unaffected by these features. Nanostructured composite materials often show a decrease in κ through effective phonon scattering. In germanium antimony tellurides (GST materials) with cobalt germanide precipitates, for example, nanostructuring of the GST phase enables zT up to 1.8 at 500 °C.[7,8] Furthermore, mixed ionic-electronic conductors (MIECs) and superionic phases represent promising thermoelectric materials according to the phonon-liquid electron-crystal (PLEC) concept, which was first described for Cu_2Se,[9] where the entropy change at the phase transition

from an ordered to a superionic structure (17 J K^{-1} mol^{-1}) is in the range melting entropies. As this high increase in entropy is caused by the disorder and mobility of Cu atoms in the crystal structure, this phenomenon has been called "liquid-like behavior".[9] However, atom hopping time scales determined by neutron scattering indicate that scattering at mobile Cu atoms affects a rather small number of phonon modes.[10] Further typical examples for this class of materials include $Zn_{13-\delta}Sb_{10}$,[11] $Cu_{12+x}Sb_4S_{13}$,[12] Cu_7PSe_6,[13] Ag_8SnSe_6,[14] and $AgCrSe_2$.[15]

The determination of the transport properties that are necessary to calculate the thermoelectric figure of merit $zT = S^2\sigma T/\kappa$ (where S is the Seebeck coefficient and T the temperature) is usually carried out under conditions different from actual ones under application. In a working Peltier cooler, the flowing DC current and thus the applied voltage are much higher than in typical measurement devices. For the determination of S of bulk materials, a small but stable temperature gradient is usually applied and the generated voltage is measured directly. In thermoelectric generator modules and Peltier coolers, the maximum thermal gradient is much greater than during thermoelectric measurements where it is approximately 50 K in typical setups. Therefore, it is possible that materials show promising properties under measurement conditions but fail in application. Concerning MIECs, electromigration is a huge problem. Simple tests on Cu_2Se, in which a constant current of 10 A was applied to the material, revealed the formation of Cu whiskers and cracks near the negative pole.[16] Similar behavior was observed for Cu_2S.[17] Recent reports discuss that metal deposition can be avoided if a critical voltage characteristic for a specific material is not exceeded.[18] For example, segmented legs have been suggested. Dividing a whole leg into three parts separated by carbon paste lowers the potential at each segment, which impedes decomposition [18] but introduces the drawback of an increased dissipation at the contact zones, which effectively lowers the application performance. However,

it remains an open question why the potential difference itself seems more important than the electrical field.

$Zn_{13-\delta}Sb_{10}$ is another prominent representative of PLEC materials.[11] Much work has been devoted to the determination of the exact composition of this phase and showed that the non-stoichiometric description $Zn_{13-\delta}Sb_x$ ($\delta = 0.28 – 0.38$) is more realistic than the classical formula Zn_4Sb_3.[19,20,21] At room temperature (RT), β-$Zn_{13-\delta}Sb_{10}$ crystallizes in space group $R\bar{3}c$ with two different atom positions for Sb^{-III} and dumbbells with Sb^{-II} as shown in Fig. S1 (S denotes Figures and Tables in the *Supporting Information*). The Sb^{-III} site forms hexagonal layers that are stacked in a way that voids form channels in the crystal structure, which are filled with Sb^{-II} dimers. Zn atoms occupy four Wyckoff sites that are close to each other, three with occupancies of only 4-6%.[11] $Zn_{13-\delta}Sb_{10}$ exhibits a remarkably high zT value of ~1.3 at 400 °C,[22] which can be explained by a combination of Zn mobility between interstitial sites as investigated by tracer experiments [23] and associated local distortions in the crystal structure, all of which apparently lead to low κ_{ph}.[24] Several notations for the low-temperature phases have been published;[25] however, α' – α – β are most frequently used in literature.[24] A phase transition from rhombohedral β-$Zn_{13-\delta}Sb_{10}$ to triclinic α-$Zn_{13-\delta}Sb_{10}$ occurs at ca. –20 °C, whose Sb substructure is similar to that of the β phase. However, it features 26 independent Zn positions, 21 of which correspond to those of the β-phase that exhibit high site occupancies. The five remaining ones describe ordered "clusters" that form pairs around centers of inversion. Below –38 °C, the modulated structure of α'-$Zn_{13-\delta}Sb_{10}$ coexists with α-$Zn_{13-\delta}Sb_{10}$.[24]

$Zn_{13-\delta}Sb_{10}$ was investigated *operando* under temperature gradients of several hundred K by transmission electron microscopy,[26] where Zn is formed at the cold side, leaving ZnSb and $Zn_{13-\delta}Sb_{10}$ in the remaining sample. The Seebeck voltage may cause electromigration in such

small samples. The application of currents > 1 A to bar-shaped samples also leads to formation of Zn and ZnSb,[27] associated with lower σ compared to $Zn_{13-\delta}Sb_{10}$ and Zn deposition at the negative pole. Increased Seebeck coefficients can be explained by the formation of ZnSb, which features a higher Seebeck coefficient than $Zn_{13-\delta}Sb_{10}$.[28] Further investigations showed that $Zn_{13-\delta}Sb_{10}$ is not stable against current-assisted sintering.[29,30] Measurements of thermoelectric properties have proved difficult as $Zn_{13-\delta}Sb_{10}$ decomposes during thermal cycling and as a consequence of the current used for the measurement of electrical conductivity. Without temperature gradients and electrical currents, $Zn_{13-\delta}Sb_{10}$ is thermally stable up to ~350 °C and then decomposes into Zn and ZnSb.[24]

Remaining questions concerning the behavior of $Zn_{13-\delta}Sb_{10}$ are: (i) At which current densities and/or voltages and/or electrical fields does Zn migration start and how does it affect the local composition? (ii) Can Zn migration be prevented by choosing low voltages or current densities and how is it affected by thermal gradients? (iii) Does a concentration gradient develop along the sample as it can be seen in $Cu_{1.97}S$,[18] and how does this affect thermoelectric properties? (iv) Which factors determine the quantity of deposited elemental Zn?

2. Experimental

2.1 Synthesis. Samples were synthesized from the elements (Zn pearls, 99.999 %, and Sb pieces, 99.9999 %, both VEB Spurenelemente, Freiberg, Germany). Stoichiometric mixtures were heated to 900 °C at a rate of 120 K h^{-1} in a vertical tube furnace. To prevent oxidation, the synthesis was carried out in silica glass ampules sealed after evacuating to ~ 5 x 10^{-3} mbar and flushing with Ar. After one day at 900 °C, samples were slowly cooled at 50 K h^{-1} in order to prevent thermal diffusion of Zn due to a thermal gradient in the sample. Different Zn:Sb ratios

were explored; a molar 4:3 ratio led to samples with Zn whiskers on the samples surface but not inside the ingots. This excess Zn could be easily separated by polishing the ingot with SiC abrasive paper (particle size 20 µm). The obtained polycrystalline samples show metallic luster and can be cut and polished without breaking.

2.2 Powder X-Ray Diffraction (PXRD). PXRD at RT was carried out using a Huber G670 diffractometer (Gunier geometry, image-plate detector with integrated read-out system) with Cu-$K\alpha_1$ radiation (Ge(111) monochromator, λ = 1.54051 Å). A representative part of the ingot was finely crushed in an agate mortar. Powder samples were placed on Mylar foils and fixed with hair-fixing spray. The software package TOPAS 5.0 was used for Rietveld refinements.[31] A fundamental parameter approach was used to describe peak profiles, including second-order spherical harmonics for preferred orientation.

2.3 Electron microscopy and energy-dispersive X-ray (EDX) spectroscopy. A LEO 1530 (Gemini, Zeiss, Germany) scanning electron microscope (SEM) was used to generate images from secondary (SE) and backscattered (BSE) electrons. Chemical analysis was carried out by EDX (INCA system, Oxford Instruments, U.K., with associated Software package).[32] The composition of the samples after applying temperature gradients and currents was determined in a space-resolved manner by determining the composition of areas of ~200 x 400 µm. Artifacts caused by surface roughness were avoided by polishing the samples (VibroMet2 polishing device, ITW Test & Measurement GmbH, Germany) with a polishing emulsion of 1 µm Al_2O_3 grains in deionized water.

2.4 Measurement of electronic and thermal transport properties. Seebeck coefficients S and electrical conductivities σ were measured simultaneously with a LSR-3 instrument (Linseis, Germany) under static He atmosphere (0.05 bar relative pressure at RT) with a temperature

gradient of 25 K and a current of 100 mA. A four-point measurement is realized by two Ni electrodes and two Ni/Cr-Ni thermocouples in a bipolar setup (continuous reversal of the electrical polarity). Measurements were carried out on bar-shaped samples, which were cut out of the ingots with a diamond wire saw (model 3242; Well, Germany). The sample surface was polished with SiC powder (grain size 5 µm). The uncertainty of both S and σ are about 10% of the measured value. Measurements of thermal diffusivity were done with a Linseis LFA 1000 laser flash apparatus equipped with an InSb detector under a static He atmosphere (0.05 bar relative pressure at RT). Heat loss and finite pulse corrections were performed applying Dusza's model.[33] Five measurements were averaged for each temperature. Thermal conductivity κ was calculated by multiplying thermal diffusivity with the Dulong-Petit heat capacity, which is consistent with experimental values,[22] and the densities of the sample, which were determined by the Archimedes method using deionized water as reference liquid. The uncertainty of κ is ~5% so that the absolute uncertainty of the given zT values amounts up to 20%.

2.5 Stress tests with currents applied under different thermal gradients. In order to investigate the stability under thermal gradients and current flow, a setup was developed (Fig. S2), which consists of a resistivity heater (Bach Resistor Ceramics, Germany) and a water cooler at opposite sides. Both are attached to copper plates for electrical and thermal contact and graphite electrodes between the copper and the sample. One can apply different voltages and temperatures on the hot side while keeping the temperature at the cooled side constant. The setup is placed in an acrylic glass chamber that can be filled with N_2. Since $Zn_{13-x}Sb_{10}$ is a p-type conductor,[11] the negative pole was connected to the hot side of the sample, where the highest positive potential of a running thermoelectric module is located. Larger amounts of Zn deposited at the negative pole were detached and their mass was determined with a precision scale

(Satorius, Germany). The resistance of the setup requires approximately 10 times the voltage for a constant current flow compared to a hypothetical setup where the sample is the only resistor. The voltages U_{start} at the start of the experiments were calculated from the shape of the samples and the measured electrical conductivities. In case of samples with a temperature gradient, an average value of the electrical conductivity was used. Details of selected stress tests are given in Table S3.

2.6 Seebeck microprobe. Local **s**canning of *S* was frequently used for characterizing the functional homogeneity of different thin-film and bulk thermoelectric materials.[34-37] A hot probe method for local thermopower scanning indicated an anisotropic Seebeck effect polycrystalline samples of $Zn_{13}Sb_{10}$ that exhibit preferred crystallite orientations owing to synthesis by a gradient-freeze technique.[38] In the present study, *S* was measured in a spatially resovled manner on bar-shaped samples of $Zn_{13}Sb_{10}$ using a Potential-Seebeck Microprobe (PSM). Basically, the PSM consists of a heated tungsten-carbide tip, a three-axes positioning system (Linos, Germany) and a data acquisition system (Keithley, USA). The sharp apex of the scanning tip ensures a small contact radius of 3 µm. The tip is positioned onto the sample surface and creates a local temperature gradient so that a thermovoltage is generated according to the temperature field, which corresponds to a local resolution of ~50 µm.[39] *S* is determined through a thermovoltage measurement by two thermoelectric circuits with the use of thermocouples (Labfacility, UK) attached to the scanning tip and the sample holder, respectively. The uncertainty of *S* on homogeneous samples areas depends on κ and equals 10-25%. However, relative changes of *S* can be detected with a much lower uncertainty of 1-3%. The samples were clamped within the vise-like PSM sample holder, which simultaneously acts as a heat sink. The scanning step width was set to 100 µm, while the temperature difference to RT was 7 K.

3. Results and discussion

3.1 Chemical and structural analysis

Rietveld refinements for samples prepared by melting and slow cooling of stoichiometric mixture with the nominal composition Zn_4Sb_3 and removing all elemental Zn at the surface show that this synthesis affords phase-pure samples. The structure model for $Zn_{13-x}Sb_{10}$ ($x \sim 0.23$) with four Zn atom positions was taken as starting model.[11] The refinement of lattice parameters and isotropic atomic displacement parameters yielded convincing agreement between the measured diffraction pattern and published models. Plots and further details of the Rietveld refinements are shown in Fig. S3 and Tables S2 and S3.

SEM-EDX measurements for a typical sample yielded 56.4(4) at.-% Zn and 43.6(4) at.-% Sb (averaged from 15 measured points), which corresponds to $Zn_{12.8(3)}Sb_{10}$. Measurements on further samples showed insignificant variations of the composition that lie in the stability range of $Zn_{13-\delta}Sb_{10}$ with $\delta = 0.22$-0.38.[21] For the sake of simplicity, the composition of our samples is given as $Zn_{\sim 12.8}Sb_{10}$. SEM images of typical samples (Fig. S4) do not show impurity phases.

3.2 Thermoelectric characterization. Measurements of thermoelectric properties underline the stability problems of $Zn_{\sim 12.8}Sb_{10}$ upon thermal cycling (Fig. S5). The peak zT value of ~0.7 at 200 °C matches with published values.[40] The evolution of S and σ over six heating and cooling cycles up to 200 °C shows that both quantities decrease during thermal cycling. These trends correspond to those reported for decomposed Zn_4Sb_3 with elemental Zn as a side phase resulting from current-assisted sintering.[30] Thermal conductivity does not vary significantly between the different heating and cooling cycles and differs between 0.6 and 0.7 $Wm^{-1}K^{-1}$ as function of temperature which also matches published values.[40]

3.3 Stability of $Zn_{\sim 12.8}Sb_{10}$ under current flow at RT

Tentative stress tests of $Zn_{\sim 12.8}Sb_{10}$ at RT employing a current density J of 180 A/cm^2, which corresponds to currents I of 10 A in typical samples (~ 8 x 2 x 2 mm) lead to the formation of cracks after a few seconds; samples disintegrate, resulting in small pieces. Current densities J = 72.2 A/cm^2, corresponding to U_{start} = 0.1495 V and an electrical field of 17.2 V/m lead to the formation of cracks after ~15 min. Zn whiskers grow at the negative pole as well as in the cracks. Near the positive pole, EDX yields Zn concentrations of 50 – 52 at.-%, which indicate ZnSb as the main phase. As ZnSb exhibits S = 370-400 µV K^{-1} at RT,[41] this is consistent with local Seebeck coefficients that are about 4 times higher than in areas with the original composition of $Zn_{\sim 12.8}Sb_{10}$ (Fig. 1). Along the whole sample, lower Zn concentrations correlate with higher Seebeck coefficients. Toward the negative pole, there is a part of the sample where the initial composition of $\sim Zn_{12.8}Sb_{10}$ is not significantly changed, followed by a crack. At the crack and at the negative pole, elemental Zn with S close to 0 µV/K is deposited. The part from the positive pole to the crack was cut into three pieces. Rietveld refinements based on the respective powder patterns (Fig. S6, Tables S4-S6) show ZnSb and $\sim Zn_{12.8}Sb_{10}$ in a ratio of 80 : 20 in the part near the positive pole and in a ratio of 44 : 55 in the middle part, where weak reflections of elemental Zn were also detected (~ 1%). Near the crack, there is exclusively $\sim Zn_{12.8}Sb_{10}$ and traces of elemental Zn.

ZnSb as a main component of decomposed parts of $Zn_{13-\delta}Sb_{10}$ samples has only been reported for currents I > 1.5 A ($J \approx$ 50 A/cm^2) under a temperature gradient of at least 200 K.[27] Reasonable current densities must be significantly lower. Fig. S7 displays Zn concentration profiles for various current densities. In fact, samples exposed to current densities of J = 2.82 A/cm^2 (I = 0.10 A, U_{start} = ~0.006 V) and J = 7.57 A/cm^2 (I = 0.20 A, U_{start} = ~0.006 V) for 10 and 5 hours,

respectively, show no visible change. However, only for the lowest current density of 2.82 A/cm^2, the Zn concentration along the sample does not vary significantly from the negative to the positive pole. At 7.57 A/cm^2, the Zn concentration near the negative pole is increased to 60 at.-% compared to 56 at.-% in Zn~$_{12.8}$Sb$_{10}$, but elemental Zn is not deposited under these conditions. Space-resolved measurements of *S* (Fig. 2) again correlate with the varying Zn concentration. *S* drops by ~6% in in the region of elevated Zn concentration. Since transported charge $Q = I \cdot t$ was kept constant for these tests, it becomes clear that higher voltages and thus current densities and electrical fields favor Zn migration.

This trend is confirmed by samples exposed current densities of 7.7 - 33.3 A/cm^2; which involve voltages of 0.016 - 0.049 V (Fig. S7). All of them show shiny Zn deposits in the form of whiskers at the negative pole and the Zn content drops to ~50 at.-% at the positive pole, i.e. ZnSb is formed like in samples treated with the higher current densities of 72.2 A/cm^3 mentioned above. As expected, in this part of the samples *S* increases drastically compared to the areas with compositions close to Zn$_{\sim 12.8}$Sb$_{10}$ that are present toward the negative pole. Typically, the Zn concentration increases continuously along the sample. Despite constant *Q*, higher current densities lead to more pronounced Zn migration in this series of experiments, too.

3.4 Stability of Zn$_{\sim 12.8}$Sb$_{10}$ under current flow in temperature gradients

Testing ~Zn$_{12.8}$Sb$_{10}$ under a temperature gradient with T_{hot} = 200 °C and currents of 0.1 – 0.2 A (J = 1.7 - 3.6 A/cm^2, U_{start} = 0.004 - 0.007 V, cf. Fig. S8) results in the formation of Zn whiskers at the negative pole (Fig. 3d - 3f and S9) in contrast to tests under comparable conditions at RT. The Zn concentration and the Seebeck coefficient vary only slightly along the remaining sample (Fig. 2e, 2f).

Further tests (Fig. S8 shows all Zn concentration profiles for T_{hot} = 200 °C) performed with constant currents I = 1 - 3 A (J = 25.0 – 68.8 A/cm^2) result in the formation of big bundles of Zn whiskers (Fig. 3a, 3b, 3c and S9). At J = 68.8 A/cm^2, which correspnds to U_{start} = 0.147 V multiple cracks with Zn whiskers are observed (Fig 4a, 4b). EDX analyses confirm that the whiskers contain only Zn and that Zn is depleted near the positive pole. Although the transported charge Q is the same in this series of experiments, the masses of deposited Zn (Table S7) differ significantly. The fact that higher current densities afford much larger Zn deposits indicates that there is no single critical voltage or current density that has to be overcome to cause Zn migration. Most likely, there are different potentials for different intersitial sites, and in addition, these may increase for lower Zn contents. As a consequence more harsh conditions are required to achieve Zn mobility in Zn-depleted material.

Current flows have a more pronounced influence when T_{hot} = 375 °C is applied. Here, constant currents of 0.10 - 0.20 A (J = 2.7 - 3.8 A/cm^2, $U_{start} \approx$ 0.009; note different sample lengths) already result in cracks with Zn whiskers and correspondingly high Zn concentration (Fig. S10). At the negative pole, the sample treated with 3.8 A/cm^2 exhibits a Zn lawn rather than whiskers. Higher currents of 2.0 A (J = 51.0 A/cm^2) and more were not feasible since the samples show cracks (Fig. 4c) and break, which stops the current flow after a few minutes.

4. Conclusion

Even at RT, $Zn_{\sim 12.8}Sb_{10}$ decomposes under the influence of electrical currents. Significant electromigration at RT starts at a current density of J = 7.6 A/cm^2, corresponding to an electrical field of 1.8 V/m. In this study, these values correspond to applied voltages of ~0.01 V and currents of 0.2 A. The formation of Zn whiskers becomes prominent at somewhat higher current

densities and voltages. In such experiments, the decrease of Zn concentration results in *S* increasing by up to 10%. When ZnSb is formed, *S* is even quadruplicated. However, Zn-rich areas also show lower values of *S* once in $Zn_{13-\delta}Sb_{10}$ the value of δ becomes negative. If elemental Zn is deposited, a Zn concentration gradient evolves along the direction of current flow. This is similar to concentration gradients observed upon exposition of copper chalcogenide MIECs to electrical fields.[18] Very high current densities of $J \geq 70$ A/cm^2 result in cracks in which Zn whiskers are formed.

Typical voltages of 0.01 V necessary to produce the critical current densities for Zn migration in $Zn_{\sim 2.8}Sb_{10}$ are much smaller than estimated critical voltages of 0.09 V for $Cu_{1.97}S$.[18] Segmented legs, which proved successful for the latter material, would be more demanding for $Zn_{13-\delta}Sb_{10}$. A sample would have to be divided in many more segments. Futhermore, the formation of cracks needs to be suppressed to render $Zn_{13-x}Sb_{10}$ applicable for thermoelectric power generation or cooling.

Decomposition phenomena become more pronounced if temperature gradients are present. The observation of Zn deposition at the negative pole indicates that the voltage needed for Zn deposition is lower at higher temperatures. However, the electrical field may be enhanced by the Seebeck voltage, which is in the same range as applied external voltages if the temperature gradients correspond to > 200 K. Features observed at RT such as concentration gradients, variations of *S* and the formation of Zn whiskers are enhanced in temperature gradients. At T_{hot} = 375 °C, the formation of cracks is observed at current densities as small as 2.7 A/cm^2.

Experiments where the transported charge *Q* is kept constant in a thermal gradient, e.g. with T_{hot} = 200 °C, show that the mass of deposited Zn depends on the current densities, which contradicts the assumption that at a certain voltage all Zn atoms start to migrate. The fact that Zn deposition

becomes more pronounced at higher voltages and current densities is indicative for a consecutive "activation" of Zn atoms in the structure of $Zn_{13-\delta}Sb_{10}$. In line with investigations on $Cu_{1.97}S$,[18] it remains an open question whether the total potential difference or the electrical field is the decisive quantity.

FIGURES

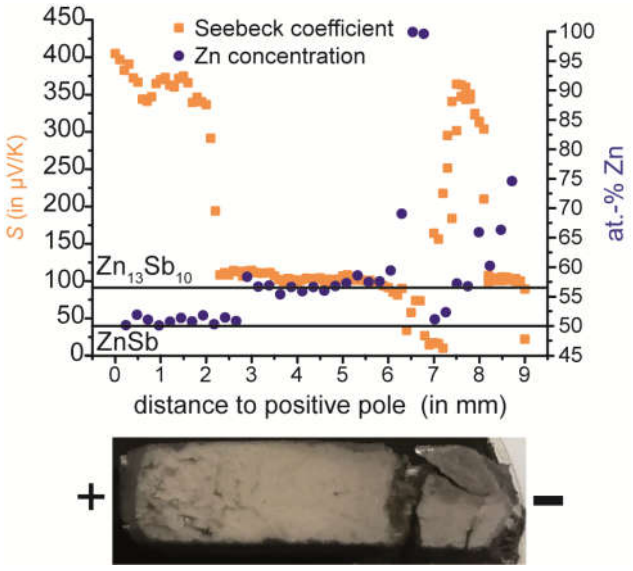

Figure 1. Zn concentration and Seebeck coefficient along a sample with visible cracks and Zn whiskers at the negative pole and in cracks; after 40 min at RT with J = 72.2 A/cm^2 (I = 4.0 A, U_{start} = 0.150 V). The magnification of the photograph correponds to the abscissa of the graph.

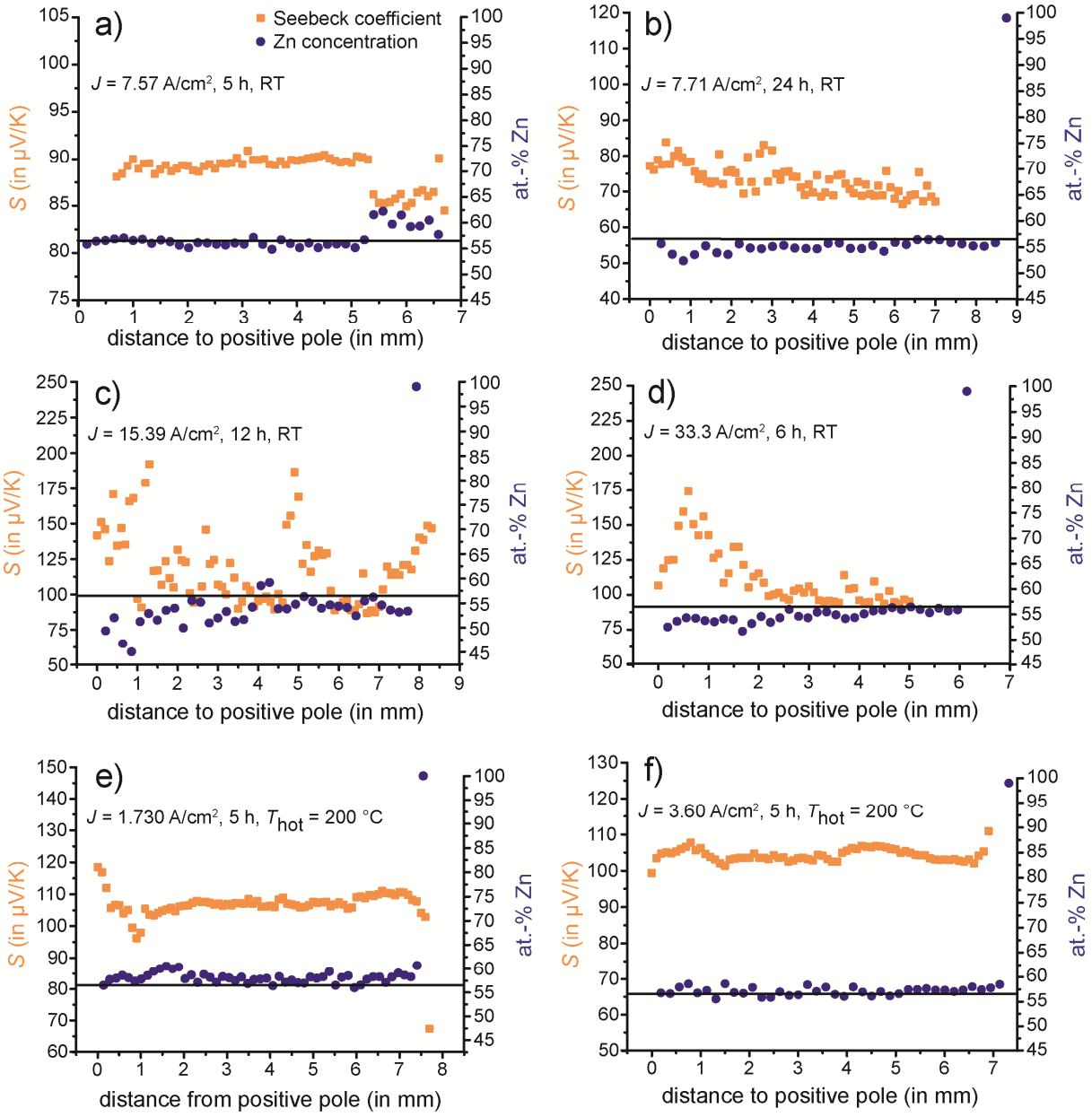

Figure 2. Zn concentration and Seebeck coefficient along the samples after current-flow experiments at RT or with a temperature gradient from RT to 200 °C: a) J = 7.57 A/cm^2, Q = 3.6·10^3 C (U_{start} = 0.012 V, I = 0.20 A, t = 5 h) at RT; b) J = 7.71 A/cm^2, Q = 21.6·10^3 C (U_{start} = 0.016 V, I = 0.25 A, t = 24 h) at RT; c) J = 15.39 A/cm^2, Q = 21.6·10^3 C (U_{start} = 0.029 V, I = 0.50 A, t = 12 h) at RT; d) J = 33.3 A/cm^2, Q = 21.6·10^3 C (U_{start} = 0.049 V, I = 1.00 A, t = 6 h) at RT e) J = 1.730 A/cm^2, Q = 1.8·10^3 C (U_{start} = 0.004 V, I = 0.10 A, t = 5 h) with T_{hot} = 200 °C; f) J = 3.60 A/cm^2, Q = 3.6·10^3 C (U_{start} = 0.007 V, I = 0.20 A, t = 5 h) T_{hot} = 200 °C. The horizontal lines correspond to the chemical composition of $Zn_{13}Sb_{10}$.

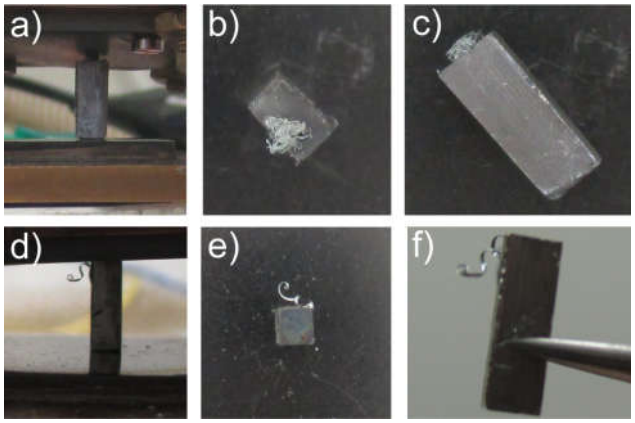

Figure 3. Photographs of $Zn_{\sim 12.8}Sb_{10}$ samples after current-flow experiments: a) b) c) 2.00 A for 40 min, T_{hot} = 200 °C. d) e) f) 0.2 A for 5 h, T_{hot} = 200 °C. a) d): after the experiment in testing setup; b) e): top view on contact plane of the negative pole/hot side; c) f): whole sample.

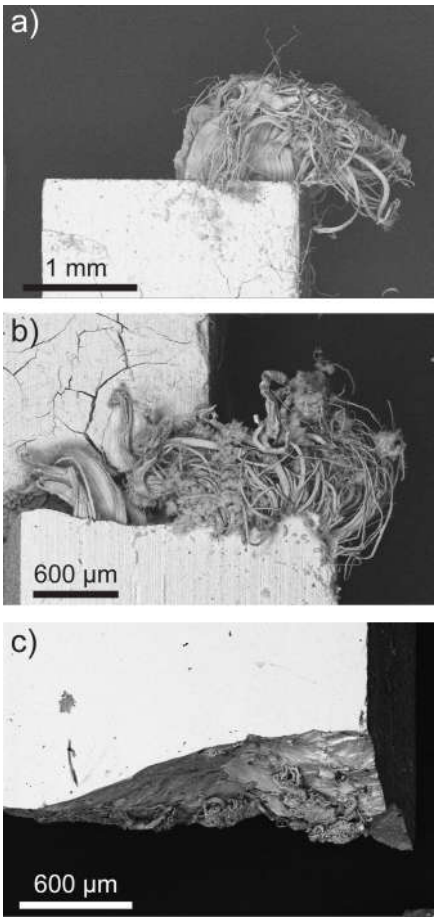

Figure 4. SEM-SE images of Zn deposits at $Zn_{\sim 12.8}Sb_{10}$ samples after current-flow experiments with J = 68.8 A/cm^2 (I = 3.00 A) for 26 min with T_{hot} = 200 °C at the hot end (a, negative pole,) and around a crack (b), respectively and (c) with J = 51.0 A/cm^2 (I = 2.00 A) for 5 min with T_{hot} = 375 °C (near a crack).

ASSOCIATED CONTENT

Supporting Information. The supporting information is available free of charge; it contains: illustration of the crystal structure of $Zn_{13-\delta}Sb_{10}$, photograph of experimental setup, details of selected tests under current flow, details of Rietveld refinements, electron microscopy images, results of thermoelectric meassurements, Zn-concentration profiles of samples after testing under current flow and different thermal gradients, estimated masses of deposited Zn.

AUTHOR INFORMATION

Corresponding Author

* Prof. Dr. Oliver Oeckler. Institute for Mineralogy, Crystallography and Materials Science; Leipzig University, Scharnhorstraße 20, 04275 Leipzig, Germany

Author Contributions

The manuscript was written through contributions of all authors. All authors have given approval to the final version of the manuscript.

Funding Sources

This research has been funded by the Operational Program of the European Regional Development Fund (ERDF) 2014-2020, project “In situ investigations on energy related materials” (project number 100357551). This measure is co-financed by tax money on the basis of budget adopted by the members of the Saxon Landtag.

ACKNOWLEDGMENT

The authors thank Rainer Sommerweiß (mechanical workshop, Leipzig University) for helping with the construction of the apparatur for the experiments under current flow and Dr. Christopher Benndorf for SEM and EDX measurements.

References

1. Shi, X.; Chen, L.; Uher, C. Recent advances in high-performance bulk thermoelectric materials. *Int. Mater. Rev.* **2016**, *61*, 379-415.

2. Yang, J.; Yip, H.-L.; Jen, A. K.-Y. Rational Design of Advanced Thermoelectric Materials. *Adv. Energy Mater.* **2013**, *3*, 549-565.

3. Zeier, W. G.; Zevalkink, A.; Gibbs, Z. M.; Hautier, G.; Kanatzidis, M.; Snyder, G. J. Thinking Like a Chemist: Intuition in Thermoelectric Materials. *Angew. Chem. Int. Ed.* **2016**, *55*, 6826-6841.

4. Slack G. A. in: CRC Handbook of Thermoelectrics (ed.: Rowe, D. M.) pp. 407–440 (CRC, Boca Raton, **1995**).

5. Nolas, G. S.; Slack, G. A. The effect of rare-earth filling on the lattice thermal conductivity of skutterudites. *J. Appl. Phys.* **1996,** *79,* 4002.

6. Schrade, M.; Berland, K.; Eliassen, S. N. H.; Guzik, M. N.; Echevarria-Bonet, C.; Sørby; M. H.; Jenuš, P.; Hauback, B. C.; Tofan, R.; Gunnæs, A. E.; Persson, C.; Løvvik, O. M.; Finstad, T.

G. The role of grain boundary scattering in reducing the thermal conductivity of polycrystalline *X*NiSn (*X* = Hf, Zr, Ti) half-Heusler alloys. *Sci. Rep.* **2017**, *7,* 13760**.**

7. Fahrnbauer, F.; Souchay, D.; Wagner, G.; Oeckler, O. High Thermoelectric Figure of Merit Values of Germanium Antimony Tellurides with Kinetically Stable Cobalt Germanide Precipitates. *J. Am. Chem. Soc.* **2015**, *137*, 12633-12638.

8. Rosenthal, T.; Schneider, M. N.; Stiewe, C.; Döblinger, M.; Oeckler, O. Real Structure and Thermoelectric Properties of GeTe-Rich Germanium Antimony Tellurides. *Chem. Mater.* **2011**, *23*, 4349-4356.

9. Liu, H.; Shi, X.; Xu, F.; Zhang, L., Zhang, W.; Chen, L.; Li, Q.; Uher, C.; Day, T.; Snyder, G. J. Copper ion liquid-like thermoelectrics. *Nat. Mater.* **2012**, *11*, 422-425.

10. Voneshen, D. J.; Walker, H. C.; Refson, K.; Goff, J. P. Hopping Time Scales and the Phonon-Liquid Electron-Crystal Picture in Thermoelectric Copper Selenide. *Phys. Rev. Lett.* **2017**, *118*, 145901.

11. Snyder, G. J.; Christensen, M.; Nishibori, E.; Calliat, T.; Iversen, B. B. Disordered zinc in Zn_4Sb_3 with phonon-glass and electron-crystal properties. *Nat. Mater.* **2004**, *3*, 458-463.

12. Vaqueiro, P.; Guélou, G.; Kaltzoglou, A.; Smith, R. I.; Barbier, T.; Guilmeau, E.; Powell, A. V. The Influence of Mobile Copper Ions on the Glass-Like Thermal Conductivity of Copper-Rich Tetrahedrites. *Chem. Mater.* **2017**, *29*, 4080-4090.

13. Weldert, K. S.; Zeier, W. G.; Day, T. W.; Panthöfer, M.; Snyder, G. J.; Tremel, W. Thermoelectric Transport in Cu_7PSe_6 with High Copper Ionic Moibility. *J. Am. Chem. Soc.* **2014**, *136*, 12035-12040.

14. Lin, L.; Liu, Y.; Dai, J.; Hong, A.; Zeng, M.; Yan, Z.; Xu, J.; Zhang, D.; Shan, D.; Liu, S.; Ren, Z.; Liu, J.-M. High thermoelectric performance of superionic argyodite compound Ag_8SnSe_6. *J. Mater. Chem. C* **2018**, *4*, 5806-5813.

15. Wu, D.; Huang, S.; Feng, D.; Li, Bing; Chen, Y.; Zhang, J.; He, J. Revisiting $AgCrSe_2$ as a promising thermoelectric material. *Phys. Chem. Chem. Phys.* **2016**, *18*, 23872-23878.

16. Brown, D. R.; Day, T.; Calliat, T.; Snyder, G. J. Chemical Stability of $(Ag,Cu)_2Se$: a Historical Overview. **2013**, *43*, 2014-2019.

17. Dennler, G.; Chmielowski, R.; Jacob, S.; Capet, F.; Roussel, P.; Zastrow, S.; Nielsch, K.; Opahle, I.; Madsen, G. K. H. Are Binary Copper Sulfides/Selenides Really New and Promising Thermoelectric Materials? *Adv. Energy. Mater.* **2014**, *4*, 1301581.

18. Qiu, P.; Agne, M. T.; Liu, Y.; Zhu, Y.; Chen, H.; Mao, T.; Yang, J.; Zhang, W.; Haile, S. M.; Zeier, W. G.; Janek, J.; Uher, C.; Shi, X.; Chen, L.; Snyder, G. J. Suppression of atom motion and metal deposition in mixed ionic electronic conductors. *Nat. Commun*. **2018**, *19*, 2910.

19. Mayer, H. W.; Mikhail, I.; Schubert, K. Über einige Phasen der Mischungen $ZnSb_N$ und $CdSb_N$. *J. Less Common Met.* **1978**, *49*, 43-52.

20. Pedersen, B. L.; Iversen, B. B. Thermally stable thermoelectric Zn_4Sb_3 by zone-melting synthesis. *Appl. Phys. Lett.* **2008**, *92*, 161907.

21. Lo, C.-W. T.; Svitlyk, V.; Chernyshov, D.; Mozharivskyj, Y. The updated Zn-Sb phase diagram. How to make pure $Zn_{13}Sb_{10}$ ("Zn_4Sb_3"). *Dalton Trans.* **2018**, *47*, 11512-11520.

22. Calliat, T.; Fleurial, J.-P.; Borshchevsky. Preperation and Thermoelectric Properties of Semiconducting Zn_4Sb_3. *J. Phys. Chem. Solids* **1997**, *58*, 1119-1125.

23. Chalfin, E.; Lu, H.; Dieckmann, R. Cation tracer diffusion in thermoelectric materials $Cu_3Mo_6Se_8$ and "β-Zn_4Sb_3". *Solid State Ionics* **2007**, *178*, 447-456.

24. Iversen, B. B. Fulfilling thermoelectric promises: β-Zn_4Sb_3 from materials research to power generation. *J. Mater. Chem.* **2010**, *20*, 10778-10787.

25. Nylén, J.; Lidin, S.; Andersson, M.; Iversen, B. B.; Liu, H.; Newman, N.; Häussermann, U. Low temperature Structural Transitions in the Phonon-Glass Thermoelectric Material β-Zn_4Sb_3: Ordering of Zn Interstitals and Defects. *Chem. Mater,* **2007**, *19*, 834-838.

26. Hung, L. T., Ngo, D.-T.; Han, L.; Iversen, B. B.; Yin, H.; Pryds, N.; Nong, N. V. In Operando Study of High-Performance Thermoelectric Materials for Power Generation: A Case Study of β-Zn_4Sb_3. *Adv. Electron. Mater.* **2017**, *3*, 1700232.

27. Kunioka, H.; Yamamoto, A.; Iida, T.; Obara, H. Electrical current dependence of the ionic conduction in Zn_4Sb_3. *Appl. Phys. Express* **2017**, *10*, 095801.

28. Pothin, R.; Ayral, R. M.; Berche, A.; Granier, D.; Rouessac, F.; Jund, P. Preparation and properties of ZnSb thermoelectric material through mechanical-alloying and Spark Plasma Sintering. *Chem. Eng. J.* **2016**, *299*, 126-134.

29. Dasgupta, T.; Stiewe, C.; Boettcher, L.; Yin, H.; Iversen, B. B.; Müller, E. Electro-migration of Zinc during current-assisted pressure sintering of β-Zn_4Sb_3 – effect of process parameters and its influence on the thermoelectric properties. *Proc. Mater. Res. Soc. Symp.* **2011**, *1325*, 137-142.

30. Yang, J.; Zhang, X.; Ge, B.; Yan, J.; Liu; G., Shi, Z.; Qiao, G. Effect of Zn migration on the thermoelectric properties of Zn_4Sb_3 material. *Ceram. Int.* **2017**, *43*, 15275-15280.

31. *TOPAS Academic*, V. 5; Coelho Software: Brisbane (Australia), **2015**.

32. *INCA Suite,* v. 4.09; Oxford Instruments Analytical Limited. United Kingdom, **1998-2007**.

33. Dusza, L. Combined solution of the simultaneous heat loss and finite pulse time corrections with the laser flash method. *High Temp.-High Pressures* **1995,** *27,* 467-473.

34. Gregory, O.J.; Amani, M. Thermoelectric Properties of $Zn_xIn_yO_{x+1.5y}$ Films. *J. Electrochem. Soc*. **2011**, *158*, J15-J19.

35. Ziolkowski, P.; Karpinski, G.; Platzek, D.; Stiewe, C.; Müller, E. Application Overview of the Potential Seebeck Microscope. *Proc. 25th ICT* **2006**, 684−688.

36. Iwanaga, S.; Snyder, G. J. Scanning Seebeck Coefficient Measurement System for Homogeneity Characterization of Bulk and Thin-Film Thermoelectric Materials. *J. Electron. Mater*. **2012**, *41*, 1667-1674.

37. Yamamoto, A.; Noguchi, T.; Obara, H.; Ueno, K.; Ikeuchi, S.; Sugawara, T.; Shimada, K.; Takasaki, Y.; Ishii, Y. Combinatorial Approach for Thermoelectric Materials through Bulk

Composition-Spreads and Diffusion Multiples. *MRS Proc.* **2007**, *1024*, 1024-A01-05; https://doi.org/10.1557/PROC-1024-A01-05.

38. Nakamoto, G.; Kurisu, M. Spatial Distribution of the Seebeck Coefficient in $Zn_{13}Sb_{10}$ determined by a Seebeck Microprobe Measurement System. *J. Electron. Mater.* **2009**, *38*, 916-919.

39. Ziolkowski, P.; Karpinski, G.; Dasgupta, T.; Müller, E. Probing Thermopower on the microscale. *Phys. Status Solidi A* **2013**, *210*, 89–105.

40. Toberer, E. S.; Rauwel, P.; Gariel, S.; Taftø, J.; Snyder, G. J. Composition and thermoelectric performance of β-Zn_4Sb_3. *J. Mater. Chem*. **2010**, *20*, 9877-9885.

41. Okamura, C.; Ueda, T.; Hasezaki, K. Preparation of Single-Phase ZnSb Thermoelectric Materials Using a Mechanical Grinding Process. *Mater. Trans.* **2010**, *51*, 860-862.